A SAR-Based Parametric Model for Tropical Cyclone Tangential Wind Speed Estimation

Sheng Wang , Xiaofeng Yang , *Senior Member, IEEE*, Marcos Portabella , Ka-Veng Yuen , Miao Zhang, and Yanlei Du

Abstract—The tangential wind speed increases from the center to the eyewall of tropical cyclones (TC) along the radial direction and begins to decay when it extends outward. The tangential wind profile model is one of the most effective and widely used methods to reconstruct the TC radial wind speed. This article proposes a parametric tangential wind profile (TWP) model based on high-spatial-resolution synthetic aperture radar (SAR) imagery. The new model functions are piecewise with maximum tangential wind speed as a threshold, and all of them are designed as nonlinear. Notably, the derivative at the segmentation threshold is zero to ensure a smooth transition of the estimated wind speed profile. With the SAR-derived azimuth-averaged wind speed, we can determine the model parameters and get the tangential wind speed. The TWP model outperforms the commonly used single-modified Rankine vortex (SMRV) model, as it better resolves the tangential wind profile shape as depicted by both SAR-derived winds and hurricane hunter stepped-frequency microwave radiometer derived winds. A comprehensive analysis of the TWP model parameters is carried out by fitting tangential winds for 620 hurricane hunter flights. Interestingly, the tangential wind profiles for major hurricanes show a similar shape. The proposed TWP model can be used for improved TC characterization and forecasting purposes.

Index Terms—Parametric modeling, synthetic aperture radar (SAR), Tangential wind speed, tropical cyclone (TC).

I. INTRODUCTION

TROPICAL cyclones (TC), one of the most violent phenomena of air-sea interaction, often bring disastrous storm surges and flooding. The knowledge of TC intensity, structure, and evolution is required to guide severe weather forecasting and risk assessment [1]. Since the gradient wind model was proposed [2], parametric models have become a powerful tool for rebuilding the TC winds. Then, with the development of numerical technology and the accumulation of research data, more and more parametric models have been established [1], [3]. These reconstructed TC winds are mainly applied to the storm surge simulation and prediction [4], [5], [6], [7], [8], [9], as well as in the forecast of TC winds and waves [6], [10], [11]. Generally speaking, the use of parametric models depends on several core parameters of the TC system, such as the maximum wind speed and its corresponding radius, and the wind distribution [12]. Therefore, one must estimate these parameters before applying a parametric model. In early model applications, these parameters were mainly obtained from buoy records [10] and aircraft flight measurements [13], [14]. However, these single or along-track observations have an obvious limitation, i.e., they do not cover the 2-D structure of TCs. The model parameters derived from these data sources cannot accurately describe the entire TC system.

Fortunately, the remote sensing observations with large spatial coverage collected from the satellite sensors overcome the mentioned limitation. Satellite sensors, such as microwave scatterometer/radiometer and synthetic aperture radar (SAR), can capture the 2-D TC structure well. Compared to the microwave scatterometer or radiometer observations [15], [16], the C-band SAR can provide quantitative information on the TC structure in both the inner and outer cores with high spatial resolution under all weather conditions [12], [17], [18], [19]. Moreover, the normalized radar cross sections (NRCSs) collected by cross-polarized SAR show the unsaturated characteristic under high wind conditions. Therefore, the *C*-band cross-polarized SAR images are suitable for parameter determination in TC modeling. Before determining TC core parameters, such as the maximum wind speed, the TC wind speed should be derived from the

Sheng Wang is with the State Key Laboratory on Internet of Things for Smart City and Department of Civil and Environmental Engineering, University of Macau, Macau 999078, China, and also with the State Key Laboratory of Remote Sensing Science, Aerospace Information Research Institute, Chinese Academy of Sciences, Beijing 100101, China (e-mail: wangsheng@radi.ac.cn).

Xiaofeng Yang is with the State Key Laboratory of Remote Sensing Science, Aerospace Information Research Institute, Chinese Academy of Sciences, Beijing 100101, China, and also with the Key Laboratory of Earth Observation of Hainan Province, Sanya 572029, China (e-mail: yangxf@radi.ac.cn).

Marcos Portabella is with the Barcelona Expert Centre, Institute of Marine Sciences, 08003 Barcelona, Spain (e-mail: portabella@icm.csic.es).

Ka-Veng Yuen is with the State Key Laboratory on Internet of Things for Smart City and Department of Civil and Environmental Engineering, University of Macau, Macau 999078, China, and also with the Guangdong-Hong Kong-Macau Joint Laboratory for Smart Cities, University of Macau, Macau 999078, China (e-mail: kvyuen@um.edu.mo).

Miao Zhang is with the Innovation Center of Xu Jianmin Meteorological Satellite, Key Lab of Radiometric Calibration and Validation for Environmental Satellites, China Meteorological Administration and National Satellite Meteorological Center, Beijing 100081, China (e-mail: zhangmiao@cma.gov.cn).

Yanlei Du is with the State Key Laboratory of Remote Sensing Science, Aerospace Information Research Institute, Chinese Academy of Sciences, Beijing 100101, China (e-mail: duyl01@radi.ac.cn).

Digital Object Identifier 10.1109/JSTARS.2022.3213822

SAR images using the inversion algorithms. The basis of these algorithms is the relationship between NRCS and wind speed. Several geophysical model functions [17], [20], [21], [22], [23], [24], [25], [26], [27], as well as a nonparametric model [28], have been established based on the cross- or dual-polarized SAR data. The workable scope of these inversion models includes both the moderate-low and high wind conditions. In particular, the latest models based on dual-polarization can retrieve wind speeds over 70 m/s [27], [28]. In summary, there are three main advantages of using the *C*-band dual-polarized SAR data to support the TC tangential wind speed modeling: the high spatial resolution captures detailed information about the TC system, which is essential for analyzing the characteristics of tangential winds and determining the model parameters; though the TCs are constantly developing and moving over time, they can be considered "static" during the SAR overpass, which typically lasts less than one minute. However, a hurricane "hunter" flight usually takes several hours to collect the directional radial measurements; and since the 2-D SAR image covers the radial winds in all directions, one can easily use the azimuth-averaged wind speed to compute the TC tangential speed.

The tangential wind profile model is the most basic method for simulating the TC radial wind speed. Usually, the most typical and most straightforward tangential wind profiles are approximated by functions that are near zero at the TC center, increase to a maximum at a particular radius value, and then asymptotically decrease to zero infinitely far from the center [29]. This assumption is consistent with the general change characteristics of TC radial wind speed. Generally speaking, there are two main types of model functions in the literature: one is designed piecewise to describe the radial wind speed in the ascending and descending segments of the tangential wind, with the segmental threshold being the maximum wind speed. The other uses a continuous function to directly describe the whole tangential winds. A series of profile models have been established in the form of piecewise functions [13], [14], [30], [31] and single continuous functions [2], [32], [33]. These two types of functions have advantages and disadvantages. Take the single-modified Rankine vortex (SMRV) model and Gaussian vortex (GV) model as examples (see Fig. 1), whose model functions are piecewise and single continuous, respectively. On the one hand, the profile of the GV model has a smooth transition at the high wind speed area. In contrast, the SMRV model has an apparent sharp inflection at the maximum wind speed. The actual TC radial wind speed at the high wind speed area does not change suddenly at a certain point but smoothly transitions within this area (see Fig. 5). Therefore, the performance of the model based on the single continuous function outperforms the SMRV at the peak wind speed region. To overcome the SMRV unsmooth transition, polynomials [30] and exponential functions [34] have been designed to describe the high radial wind speed transition near the hurricane eyewall. Although relatively smooth transition results can be obtained, the functions of these methods usually contain a series of coefficients, adding to the complexity of the model application. This means that the existing methods must sacrifice the model's simplicity to describe the wind speed profiles accurately. Besides, in most piecewise function models,
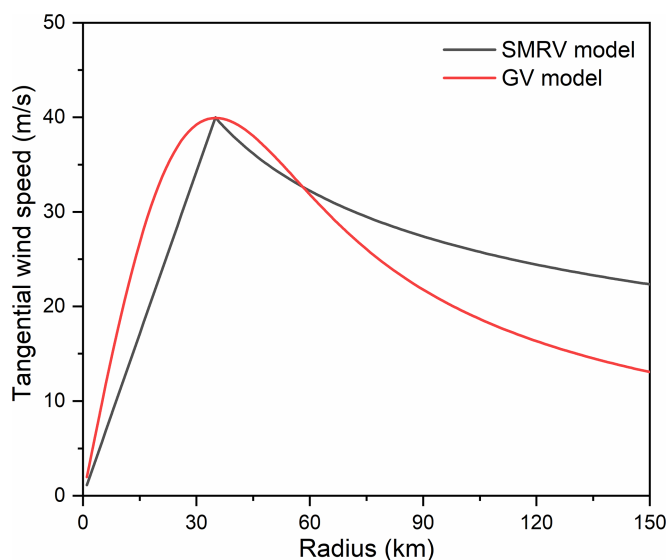

Fig. 1. Tangential wind profiles estimated by the SMRV (black) and the GV (red) models with $V_{max} = 40$ m/s and $R_{max} = 40$ km. The decay exponent in SMRV is $\alpha = 0.4$. The mathematical expressions of these two models are given in Appendix.

a linear function is used to estimate the wind speed from the TC eye to the eyewall, and the wind speed of the TC center is often set as zero. Although these assumptions and treatments are helpful for modeling, they negatively impact the accuracy of the model. On the other hand, the model based on a single continuous function describes the two segments of tangential wind speed with the same function. The estimation accuracy on the ascending section, i.e., the area from TC center to eyewall, is generally poor [12]. Because there are usually much fewer data points within the TC eyewall than in outside areas, the model parameters will be mainly determined by the data points outside the TC eye area when using the fitting method to determine them. In contrast, the model based on a piecewise function can avoid this problem by using different functions to describe these two segments.

Based on the analysis above, a novel tangential wind speed model (TWP) can be designed by exploiting the advantages of both the piecewise and the continuous functions. This means that the new model can be piecewise. Still, the defects, such as the unsmooth profile transition near the eyewall, the setting of zero of TC center wind speed, and the linear estimation of wind speed in the inner area of the eyewall, should be avoided by selecting suitable piecewise functions. Inspired by the smooth simulating profiles of the radial structure model (based on the Gaussian function) [35] and the GV model, the Gaussian-like function has the potential to be the basis of the new model functions. Therefore, a novel TWP is proposed in this article based on SAR observations. The model functions include two sections, and each one is a Gaussian-like function. Satisfactorily, the new model can accurately estimate the tangential winds with a relatively concise form, and its wind profile transition is smooth in the high wind area. The article is organized as follows. Section II introduces Sentinel-1A images, SFMR measurements, and flight-level aircraft data. Section III presents the
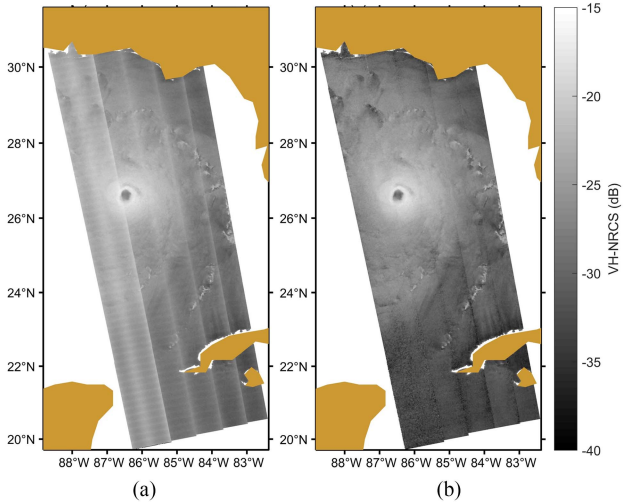
Fig. 2.   Cross-polarized SAR image over TC Michael, from 23:43 to 23:46 UTC, on October 9, 2018. (a) before denoise. (b) After denoise.

establishment of the TWP model. In Section IV, the TWP model is validated with the SMRV model and SFMR measurements, and the discussion of the model parameter is also given. Finally, Section V presents the conclusion.

II. DATASETS

A. Sentinel-1A SAR Data

The Sentinel-1A was launched in April 2014 as part of the European and operational Copernicus program space component. The C-band SAR onboard Sentinel-1A can provide single-polarized (HH or VV) and dual-polarized (VV+VH or HH+HV) backscatter measurements in four modes: interferometric wide swath; extra wide (EW) swath; strip map; and wave modes. In this article, the S-1A SAR data are the EW mode dual-polarized (VV+VH) ground range detected products. The EW mode has a swath of 400 km and an incidence angle range between 17° and 45°. Moreover, the spatial resolution and pixel spacing of EW are 93 m × 87 m (range by azimuth) and 40 m × 40 m, respectively. Here, we collect 11 dual-polarized SAR images covering 7 TCs from 2016 to 2018. For the cross-polarized measurements of these SAR images, the adverse effect of the additive noise on NRCS accuracy and the low signal-to-noise ratio is profound. The denoising method proposed in [36] and the annotated noise information in the sentinel-1 level-1 products [37] are used to remove the thermal noise that changes with the antenna pattern and the scalloping noise that varies along the azimuth direction. Fig. 2 shows an example before and after the denoise procedure, showing promising results after denoising.

B. SFMR Measurements

The stepped-frequency microwave radiometer (SFMR) onboard the National Oceanic and Atmospheric Administration (NOAA) WP-3D and U.S. Air Force aircraft is an airborne remote sensing instrument providing wind speed and rain rate

estimates. The wind speed estimate principle relies on using six different C-band frequencies, i.e., 4.55, 5.06, 5.64, 6.34, 6.96, and 7.22 GHz. SFMR measurements provide transects of wind speed with relatively high spatial (∼120 m) and temporal (1 s) resolutions. The revised SFMR processing algorithm can derive the sea surface wind speeds up to 70 m/s [38]. In this article, the collocated SFMR winds for TCs Irma (2017), Michael (2018), and Hector (2018) are used for model validation. To ensure enough spatiotemporal matched SFMR data are collected, we use a 3-h temporal window. Since there is a difference in the acquisition time between SAR images and SFMR measurements, we use SFMR in storm-motion coordinates, which assumes that the structure of the hurricane with respect to the storm motion direction does not significantly vary over the pre-defined time window. For such purpose, we use the best track data provided by the U.S. National Hurricane Center (NHC) (http://www.nhc.noaa.gov/data/#hurdat) to correct the spatial position of SFMR data by the time difference.

C. Flight-level Aircraft Data

The flight-level aircraft data of Atlantic and eastern Pacific TCs between 1977 and 2011 is provided by NOAA-Hurricane Research Division archive. The dataset consists of radial legs of data obtained as the aircraft performs repeated penetrations and exits of the TC core through the storm center. The different storm quadrants are usually well covered by radial legs of data because the data are typically obtained from one or more complete or partial "figure-four" flight patterns, most often in the N–S–E–W or NW–SE–NE–SW direction during one single flight mission. It is noted that the average flight mission typically lasts 6 h and results in eight radial legs of data. Generally, the flight-level data are collected when the flight is performed at standard pressure levels. The collocated dataset comprises radial data legs from the storm center to a maximum 150-km radial extent with 0.5-km grid spacing. Each radial data was converted to storm motion-centric coordinates after the original raw wind data was recomputed in a cylindrical-polar coordinate system moving with the cyclone center [13], [14]. In this article, the azimuth-averaged tangential wind speed is calculated with the available radial legs of data obtained during a single flight mission. Finally, 4106 radial legs of data were obtained from 620 flight missions for 76 hurricanes. An example is shown in Fig. 3 with the tangential wind profiles of hurricane Floyd (1999) obtained on September 12, 1999.

III. ESTABLISHMENT OF TWP MODEL

A. Design of TWP Model

As discussed in previous sections, the new TWP model is designed as a piecewise function with the form of Gaussian-like functions. The piecewise threshold of the function is consistent with the classical SMRV model (see Appendix), i.e., the corresponding radius at the maximum wind speed of azimuth-averaged tangential wind speed. Considering the enhancement-weakening process of the tangential wind inside and outside the TC eyewall, the growth parameter a and the decay parameter b
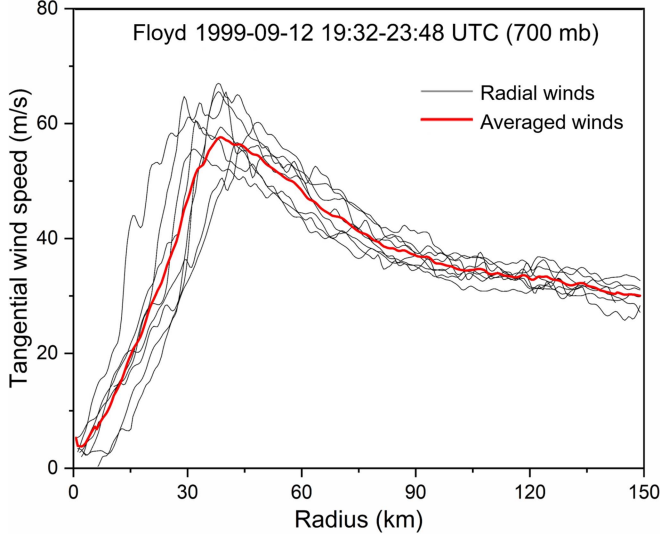
Fig. 3. Tangential wind profiles at 700 mb for Floyd (September 12, 1999, UTC 17:32-23:48), which include eight radial profiles (black lines) selected from the flight-level dataset and the azimuth-averaged one (red line).

Fig. 4. Tangential wind profiles for different combinations of parameters a and b with $V_{\max} = 40$ m/s, $R_{\max} = 35$ km.

are used in the model functions in (1). In addition, a constant value of 1 is added to the functions based on mathematical considerations so that the two parts of the functions have the same shape, i.e., with zero derivatives, at the segmentation point ($R_{\max}$). Therefore, the TWP model can be formulated as

$$V = \begin{cases} V_{\max} \exp\left(-\left(\frac{1}{a}\left(\frac{r}{R_{\max}} - 1\right)\right)^2\right) & r \leq R_{\max} \\ V_{\max} \exp\left(-\left(\frac{1}{b}\left(\frac{R_{\max}}{r} - 1\right)\right)^2\right) & R_{\max} < r \leq 150 \text{ km} \end{cases}$$

(1)

where $V_{\max}$ is the maximum wind speed of the azimuth-averaged tangential wind speed; $R_{\max}$ is its corresponding radius; r is the distance to the hurricane center. Moreover, the reason for choosing the unity constant term is that the radius ratio ($r/R_{\max}$ or $R_{\max}/r$) ranges from zero to one. In this way, the first segment of the function monotonically increases while the second monotonically decreases, which well fits the changing trend of the tangential winds. More importantly, the derivatives at the maximum wind speed ($r = R_{\max}$) are zero, thus ensuring a smooth transition of the wind profiles. Fig. 4 shows the tangential wind speeds calculated with different value combinations of the parameters a and b. For the ascending segment of these profiles, the value of parameter a controls the rate of increase of the tangential wind inside the eyewall. The greater the value of parameter a, the stronger the wind speed at the TC center ($r = 0$), but the slower the wind speed growth. Similarly, as seen from the descending part of these profiles, the value of parameter b controls the rate of decrease of the tangential wind outside the eyewall. Therefore, using the different value combinations of a and b we can describe the different TC cases.

B. Parameters Estimation

The determination of model parameters depends on the wind speed of the TC. Here, the SAR co-polarized and cross-polarized
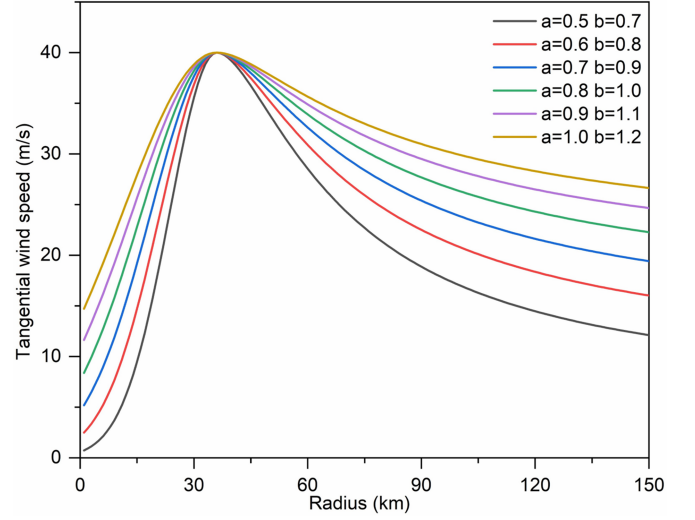
measurements are combined to get the wind speed using the modified model based on sentinel-1A data for hurricane winds (MS1AHW) [27]. The inversion calculation can be regarded as the minimization problem of the cost function to obtain a wind vector

$$J(u_{10}, v_{10}) = \left[\frac{\sigma_0^{VV} - \text{CMOD5}.N(\theta, \phi, |\boldsymbol{U}_{10}|)}{\Delta\sigma_0^{VV}}\right]^2$$
$$+ \left[\frac{\sigma_0^{VH} - \text{MS1AHW}(\phi, |\boldsymbol{U}_{10}|)}{\Delta\sigma_0^{VH}}\right]^2$$
$$+ \left[\frac{u_{10}^{\text{ECMWF}} - u}{\Delta u_{10}}\right]^2 + \left[\frac{v_{10}^{\text{ECMWF}} - v}{\Delta v_{10}}\right]^2 \quad (2)$$

where $\text{CMOD5}.N(\theta, \phi, |\boldsymbol{U}_{10}|)$ and $\text{MS1AHW}(\phi, |\boldsymbol{U}_{10}|)$ are the radar cross section values simulated from the CMOD5.N and MS1AHW model, respectively. σ_0^{VV} and σ_0^{VH} are the co-polarized and cross-polarized NRCS of SAR data, respectively. The wind speed $|\boldsymbol{U}_{10}|$ is defined from 0 to 80 m/s with a step of 0.1 m/s. The incidence angle ϕ is defined from $17°$ to $45°$ with a resolution of $0.1°$. The wind direction θ with respect to the azimuth angle is defined from $0°$ to $360°$ with a resolution of $0.5°$. Then, u and v components are calculated as $u = |\boldsymbol{U}_{10}|\cos(\theta)$ and $v = |\boldsymbol{U}_{10}|\sin(\theta)$. The u_{10}^{ECMWF} and v_{10}^{ECMWF} are the wind components of the European Centre for Medium-Range Weather Forecasts (ECMWF) wind vector with a spatial resolution of $0.125°$ and time steps of 3 hours. $\Delta u_{10} = \Delta v_{10} = 2$ m/s, $\Delta\sigma_0^{VV} = 0.1$. The $\Delta\sigma_0^{VH}$ is defined by the signal-to-noise ratio. We determine the optimum $|\boldsymbol{U}_{10}|$ by minimizing the cost function in (2) iteratively.

The wind speed is derived from the SAR images using the retrieval model mentioned above. Then the tangential wind profile is calculated by averaging the wind speed in all azimuthal directions. We determine the $V_{\max}$ and corresponding $R_{\max}$ from the averaged profiles. Next, the SAR-derived wind speed is divided into two groups with $R_{\max}$ as the threshold. Finally, model parameters a and b are determined by fitting the two

TABLE I
MODEL PARAMETERS COMPUTED FROM THE 11 SAR IMAGES

TC Name	Date	Time (UTC)	Hurricane Center		V_{max} (m/s)	R_{max} (km)	a	b	α
			Lat	Lon					
Lyonrock	August 28, 2016	20:50	136.08°E	25.67°N	48.52	27	0.57	1.1	0.33
Karl	September 23, 2016	22:20	65.34°W	29.99°N	25.04	69	1.22	1.14	0.27
Megi	September 26, 2016	09:33	125.61°E	21.50°N	50.49	64	0.92	1.02	0.35
Irma	September 7, 2017	10:30	68.65°W	20.00°N	64.02	26	0.74	0.91	0.51
Hector	August 7, 2018	15:43	147.85°W	16.13°N	55.77	19	0.64	0.75	0.68
	August 28, 2018	04:13	151.12°W	16.43°N	51.75	17	0.71	0.77	0.63
Florence	September 4, 2018	08:36	41.39°W	19.36°N	23.09	36	0.76	1.05	0.36
	September 7, 2018	21:32	52.51°W	24.62°N	15.95	51	0.99	1.82	0.12
	September 8, 2018	09:38	53.96°W	24.71°N	22.42	21	0.84	1.47	0.18
Michael	October 9, 2018	23:43	86.50°W	26.55°N	53.52	28	0.55	0.78	0.66
	October 10, 2018	11:49	86.31°W	28.98°N	54.89	28	0.77	0.84	0.57

wind groups with the model function listed in (1). Recently, Zhang et al. [39] proposed a parameter determination method based on the least-squares fit method for extracting parameters of tangential wind models from SMAP data. Different from piecewise fitting the model function, [39] uses all data points to fit two parts of the model function simultaneously to reduce the influence of the uneven distribution of the number of data points from the inner and outer eyewall regions. When using this method to determine the model parameters, different model functions will lead to different R_{max} and V_{max} for the same TC case. However, for a specific TC case, these two parameters should be unique because they are only depended on the TC system itself instead of the model functions. Specifically, these two parameters are the general ones for TCs, while parameters a and b in the TWP model and α in the SMRV model are unique parameters from the corresponding models. Therefore, we extract the general parameters from the azimuth-averaged wind speed. Then, we use the piecewise function to fit all data points in the corresponding groups divided by R_{max} to determine the unique parameters from models. However, it is not always efficient to use the azimuth-averaged to determine the model parameters. For the high-spatial-resolution SAR data, there are adequate data points to determine the azimuth-averaged profile and corresponding model parameters. But for the observations with low spatial resolution, e.g., the SMAP wind products, it is challenging to obtain R_{max} and V_{max} directly and accurately. In these scenarios the method in [39] is a better choice to determine the model parameters.

The determination of the TC center is a basis for calculating the averaged wind speed profiles. In this article, we use the best track provided by NHC to determine the TC center considering the simplicity of calculations. First, we use the best track records closest to the SAR acquisition time to calculate the TC's moving speed and direction. Then, the position of the TC center at the SAR acquisition time is determined according to the time difference between the SAR acquisition time and the best track data. Some other methods can also locate TC centers based on satellite observations, such as using a threshold methodology from the original SAR image [31] and finding the best TC center associated with SMRV parameters by moving the candidate centers one-by-one from SMAP observation [39].

With the wind speed derived from the 11 SAR images and the TC centers calculated from best track data, the radial distributions within 150 km of the TC center are shown in Fig. 5. The red lines represent the azimuth-averaged wind speeds. Thus, we determine the parameters R_{max} and V_{max} with them, and further calculate the parameters a, b, and α using the data groups divided by the R_{max}. The results are given in Table I. As seen in Fig. 5, around the wind speed peak of these profiles, there is no apparent sharp inflection but rather a smooth transition for all cases. In the ascending parts of the profiles, corresponding to the area inside the TC eyewall, the tangential wind speed usually increases nonlinearly, and the curve significantly differs from one case to the next. Hence, in contrast with nonlinear TWP models, a linear function like that of the traditional models (e.g., the SMRV model) does not represent these tangential winds well. In the descending part of the profiles, the wind speed decreases nonlinearly with a slower rate from the TC eyewall to the periphery. Moreover, comparing the distribution of the tangential wind speed of these cases, we can find their shapes are quite different. For the cases of Fig. 5(b)–(d), the distribution of scattered points is looser than in other cases. For a certain radius, the corresponding wind speed has multiple values. The asymmetry of TCs mainly causes this difference. Recently, a morphology model for the TC inflow angle asymmetry is proposed to estimate surface wind vectors [40], which can be used to describe the asymmetry of TC wind speed. For the azimuth-averaged profiles, there is an obvious difference between the cases in Fig. 5, especially in the ascending part. Take Fig. 5(b), (d), and (e) as examples, the radius corresponding to the maximum wind speed is significantly larger than in other cases, and the ascending part of profiles in these three sub-figures change more smoothly.
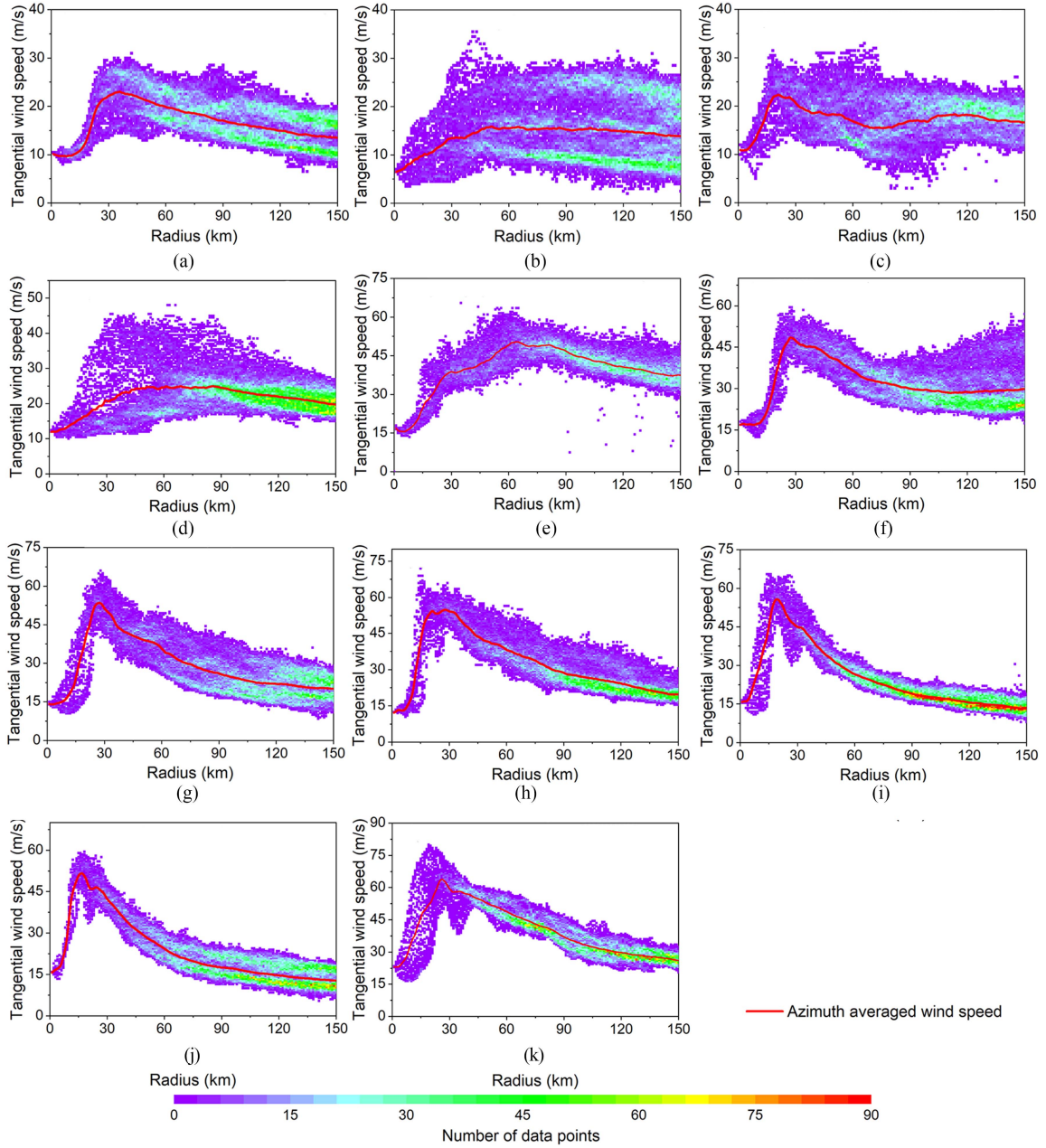
Fig. 5. SAR-retrieved wind speed distributions plotted as a function of the TC radius and their corresponding azimuth-averaged wind profiles (red lines) for 11 cases. The color indicates the number of data points in each 1-km interval data bin. (a) Florence (2018-09-04 08:36 UTC). (b) Florence (2018-09-07 21:32 UTC). (c) Florence (2018-09-08 09:38 UTC). (d) Karl (2016-09-23 22:20 UTC). (e) Megi (2016-09-26 09:33 UTC). (f) Lyonrock (2016-08-27 20:50 UTC). (g) Michael (2018-10-09 23:43 UTC). (h) Michael (2018-10-10 11:50 UTC). (i) Hector (2018-08-07 15:43 UTC). (j) Hector (2018-08-08 04:13 UTC). (k) Irma (2017-09-07 10:30 UTC).

IV. RESULTS AND VALIDATIONS

A. Model Validation

Using the model parameters in Table I and (1), we can get the estimated tangential wind speed of the models. The comparison results of the tangential wind speed profiles are shown in Fig. 6. We compare these wind profiles from three aspects: the ascending part; the descending part; and the area near the peak of the profiles. The ascending portion shows two main differences between the TWP and the other two models. One is that the wind speed of the SMRV and GV models is

always zero at the TC center, but that of the TWP model is $V_m \exp((1/a)^2)$. The other is that the tangential wind speed is nonlinear by observing the azimuth-averaged profiles. Thus, the nonlinear TWP model overperforms the linear SMRV model in the ascending parts, whose wind profiles are more consistent with the azimuth-averaged ones. Though the GV model also estimates wind speed nonlinearly, its fixed model parameters make it less flexible than the other two models. Then, The results from the TWP and SMRV models are close in the descending part, while the GV model shows an obvious inapplicability. Finally, in the peak area of the profiles corresponding to the high winds near
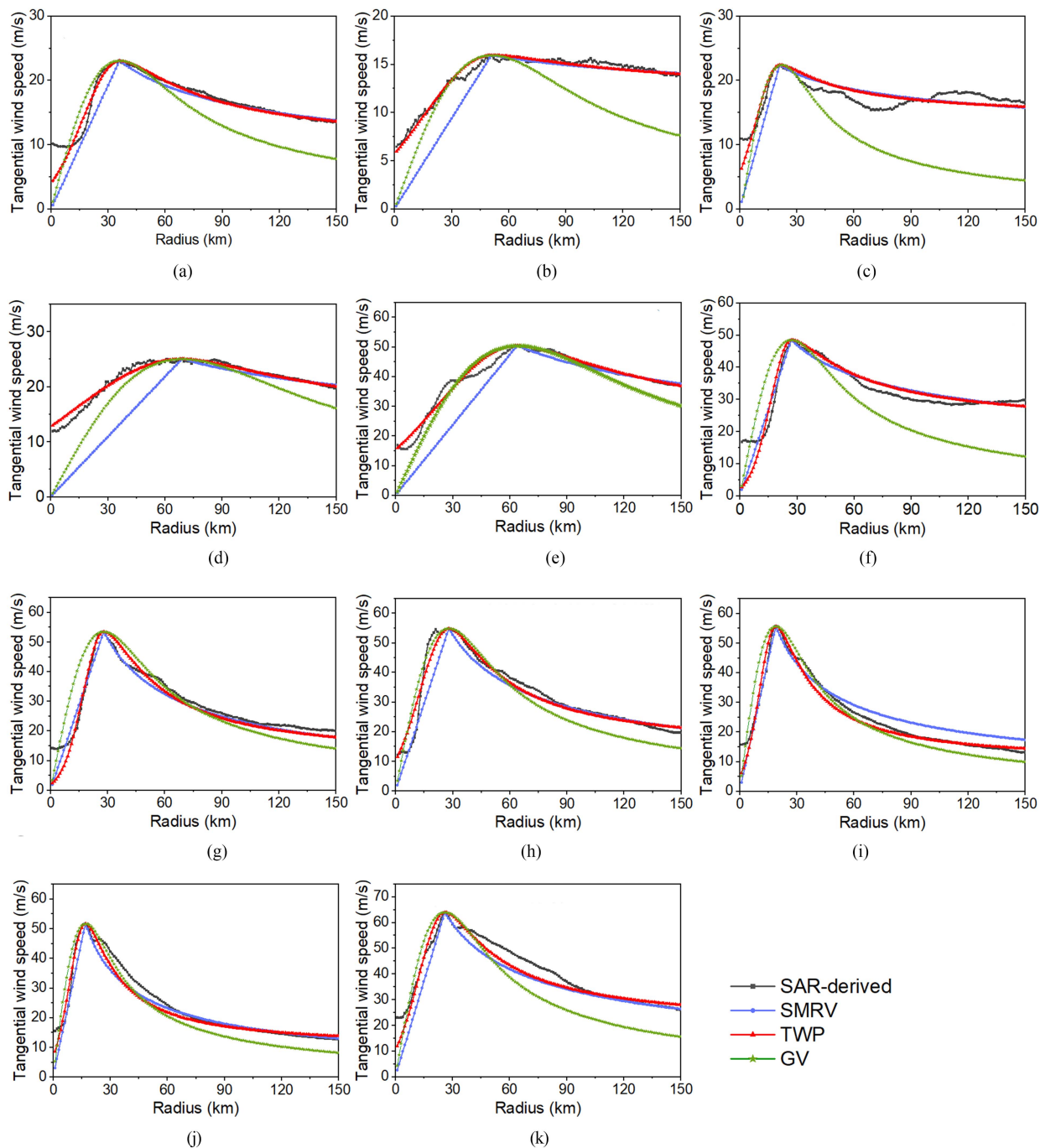
Fig. 6. Model estimated tangential wind speed profiles versus the SAR-derived azimuth-averaged ones for 11 TC cases. The lines in black, blue, red and green represent the tangential wind speed obtained from SAR images, SMRV, TWP and GV models, respectively. (a) Florence (2018-09-04 08:36 UTC). (b) Florence (2018-09-07 21:32 UTC). (c) Florence (2018-09-04 09:38 UTC). (d) Karl (2016-09-23 22:20 UTC). (e) Megi (2016-09-26 09:33 UTC). (f) Lyonrock (2016-08-27 20:50 UTC). (g) Michael (2018-10-09 23:43 UTC). (h) Michael (2018-10-10 11:50 UTC). (i) Hector (2018-08-07 15:43 UTC). (j) Hector (2018-08-08 04:13 UTC). (k) Irma (2017-09-07 10:30 UTC).

the TC eyewall, the wind speed change characteristics of these models are different. For the SMRV model, the transition of wind speed is unsmooth, forming sharp inflection points at the peak of the profiles. However, the TWP and GV models have a smooth transition in the same area because the two segments of the model function have the same form, and its derivative is zero at the peak points. Overall, the TWP model outperforms the SMRV and GV models from the comparison results of profile shape.

Due to the apparent disadvantages of the GV model, the TWP and the SMRV models are compared in the follow-up model comparison. To compare these two models quantitively, the root-mean-square error (RMSE), bias, and correlation coefficient (CC) of the model estimated wind speed against azimuth-averaged one are calculated. Fig. 7 shows the statistical results of these models for the 11 study cases listed in Fig. 6(a)–(k). Here, we use symbols (A)–(K) in the horizontal
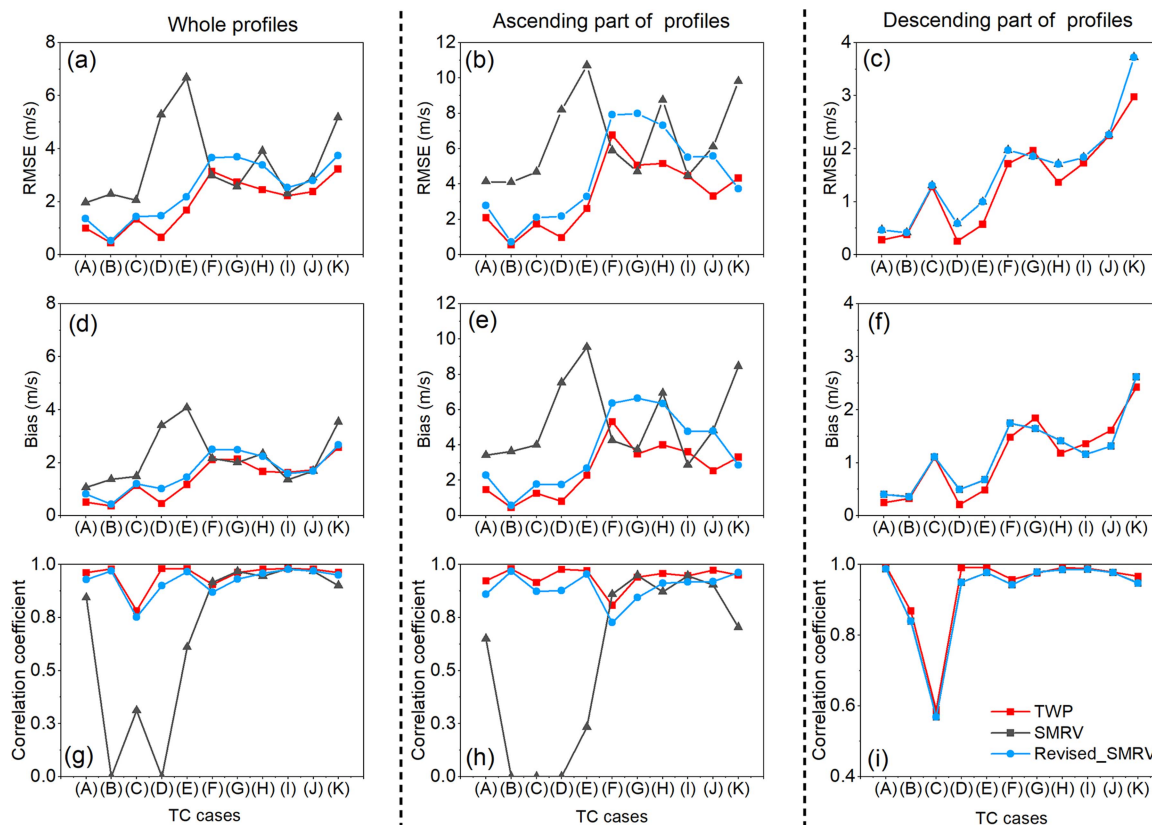
Fig. 7. RMSE, bias of the model estimated tangential wind speed against the SAR-derived one. (a) and (b) Results of whole profiles, (c) and (d) Ascending parts. (e) and (f) Descending part. The symbols (A)–(K) in the horizontal axis are represent the TC cases numbered as (a)–(k) in Fig. 5, respectively.

axis to represent corresponding TC cases in Fig. 6 numbered with lowercase (a)–(k). The first column of subgraphs in Fig. 7 shows the RMSE, bias, and CC for the whole wind profiles. Compared with the SMRV model, the TWP model has an apparent accuracy advantage for most cases. To analyze the performance difference of the models inside and outside the TC eyewall, we divide the wind profiles into two parts with the threshold of the maximum wind speed. Then the accuracy of these two parts is calculated, respectively. The second and third columns of Fig. 7 are the statistical results of ascending and descending parts, respectively. The accuracy in the ascending part is significantly lower than that in the descending part for most cases, especially for the SMRV model. The amount of data in the ascending part is lower than that in the descending part, which affects the error statistics results. The linear estimation of the SMRV model in the ascending part further increases the statistical error scores. Moreover, the subgraphs of the second column in Fig. 7 show that the TWP model overperforms the SMRV model in the ascending part, which is also the main reason for the better overall accuracy of the TWP model. For the descending part of the profiles, the accuracy difference between the two models is smaller than for the ascending part. There are two principal factors for the better performance of the TWP model: the nonlinear function can better describe the characteristics of wind speed change from the TC center to the eyewall. At the TC center, i.e., the radius is zero, the wind speed

of TWP is determined by parameter a and the maximum wind speed, but that of SMRV can only be set as zero.

To further compare the importance of these two factors, we use a revised SMRV model (see Appendix for model function) that adds the wind speed of the TC center to the first part of the SMRV model functions to validate the effects of the second factor. The statistics (RMSE, bias, and CC) of the revised SMRV model are drawn in blue dotted lines in Fig. 7. Note that the blue line (revised SMRV model) overlaps the black line (SMRV model) in the third column of Fig. 7, i.e., they are in identical. Comparing the SMRV model, the accuracy of the revised SMRV model is significantly improved w.r.t. that of the (original) SRMV model in 8 of the 11 cases. Since the wind speed at the TC center is set as an actual value instead of zero, the error of the wind speed estimated by linear functions is suppressed. Moreover, compared to the revised SMRV model, the TWP model still performs better. In detail, the statistics of these two models in Fig. 7 reveal that this accuracy advantage mainly comes from the ascending part, proving that the nonlinear fitting function also significantly contributes to the model performance. In addition, we calculate the average value of RMSE for all cases to quantitatively compare the contribution of the two factors to the model performance. Compared to the SMRV model, the RMSE of the revised SMRV is improved by 1.03 m/s for the whole profile and 2.04 m/s for the ascending part. Then, compared to the results of the revised SMRV model, the accuracy of the TWP model in
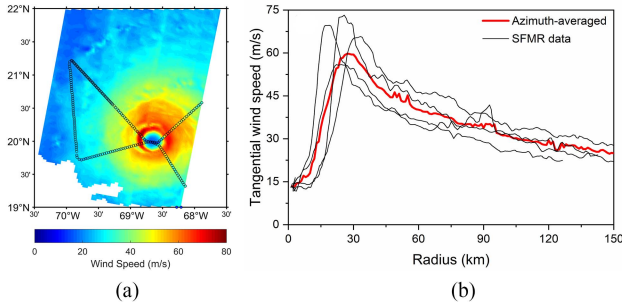
Fig. 8.   (a) SFMR tracks for TC Irma during the time window from 09:00 UTC to 13:00 UTC, September 7, 2017. (b) SFMR wind speed of four radial legs (black solid lines) and their azimuth-averaged result (red solid line).
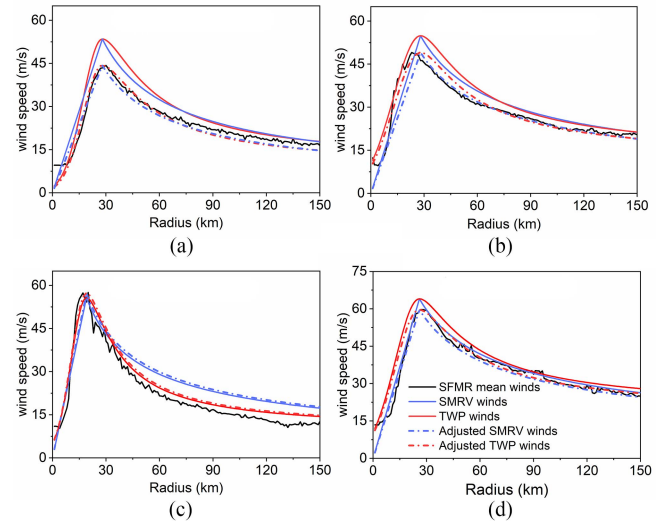

Fig. 9.   Model estimated tangential wind speed profiles versus SFMR azimuth-averaged ones for four cases. The black lines represent the SFMR results, the other lines with different colors and shapes represent the tangential wind speed estimated by models and their adjusted ones. (a) Michael 2018-10-09. (b) Michael 2018-10-10. (c) Hector 2018-08-07. (d) Irma 2017-09-07.

the whole profile, the ascending part and the descending part are improved by 0.49, 1.09, and 0.21 m/s, respectively. Therefore, if the effect of the second factor is excluded, i.e., the initial wind speed of the two models at the TC center ($r = 0$) is not zero, the TWP model based on the Gaussian function still has significant advantages due to the first factor.

To further verify the performance of the TWP model, we use the collocated SFMR measurements of TCs Irma (2017), Hector (2018), and Michael (2018) to compare with the wind speed of TWP. First, we collect the SFMR measurement with a time window of ±3.0 h. Note that the SFMR data contains the variable of quality "Flag" and only the value of it zero means the data are reliable. Thus, the low-quality data points with the variable "Flag" of not zero were filtered out. Then, these SFMR data are resampled with the spatial resolution of 1 km to be consistent with the SAR-derived winds. Second, we collect the radial legs of SFMR data across the TC center. As shown in Fig. 8(a), there are four qualified radial data for TC Irma (2017). The black lines in Fig. 8(b) represent their wind speed profiles, and the red line is the azimuth-averaged one. There are noticeable differences in these radial wind speeds in different directions, so it is reasonable to use the azimuth-averaged one to represent the tangential wind speed of the TCs. Finally, Fig. 9 compares the azimuth-averaged SFMR wind speed and that of models. However, there is an apparent underestimate of SFMR for most TC cases in Fig. 9. There are two reasons for this. One is that the azimuth-averaged SFMR results are only calculated from several radial legs of data, which is different from that derived from all directions to some certain. As shown in Fig. 8(b), although the maximum wind speed of three radial profiles is greater than 60 m/s, that of the averaged wind speed is less than 60 m/s due to the significant difference in the distribution of these radial wind speeds with the radius. In contrast, the averaged wind speed in Fig. 5 considers all radial winds, so the accidental error is suppressed to the greatest extent. Another reason is that the TCs are evolving and moving during the SFMR acquisition period, which may cause the succeeding differences in wind speeds. Here, to obtain the qualitative comparison results more intuitively, we adjust the wind speed of TWP and SMRV models according to the proportional relationship of their maximum wind speed to the SFMR one. The adjusted ones are drawn as red and blue dotted lines in Fig. 9, respectively. Note that

this adjustment of the profiles is only to compare the shape differences of the profiles at the same wind speed level, rather than to correct the accuracy of the model wind speed. Compared to the adjusted SMRV winds (blue dotted lines), the TWP ones (red dotted lines) have better good consistency with the SFMR measurements (black lines), which reveals the nontrivial capacity of the TWP model in accurately describing the TC tangential wind characteristics. Similar to the azimuth-averaged wind speed obtained from SAR images, the SFMR winds have prominent nonlinear characteristics in the inner region of the TC eyewall and show a smooth transition in the high wind speed regions. Fortunately, the TWP results successfully capture these features. Therefore, this result qualitatively confirms that the TWP model has unique advantages in accurately depicting the variation characteristics of TC tangential wind speed. Compared with the azimuth-averaged winds obtained from 2-D wind speed, the SFMR tangential wind calculated from limited radial measurements is affected by the number of radial legs and acquisition time difference, leading to inconsistent results. Thus, we do not use these SFMR data for quantitative analysis.

B. Discussion on Model Parameters

As for model application, it is relevant to analyze the distribution characteristics of parameters a and b, to provide a valuable reference during model parameter determination. Using the radial wind speed profiles obtained from the 620 flight missions, the histograms of parameters a and b are shown in Fig. 10. Accounting for the a and b different value ranges, their corresponding bins are set to 0.05 and 0.10, respectively. As shown in Fig. 10(a), the distribution of parameter a is relatively narrow, with the mean and standard deviation (Std) values of 0.80 and 0.21, respectively. In particular, the distribution ranges are [0.40, 1.70] with the maximum value at the subinterval
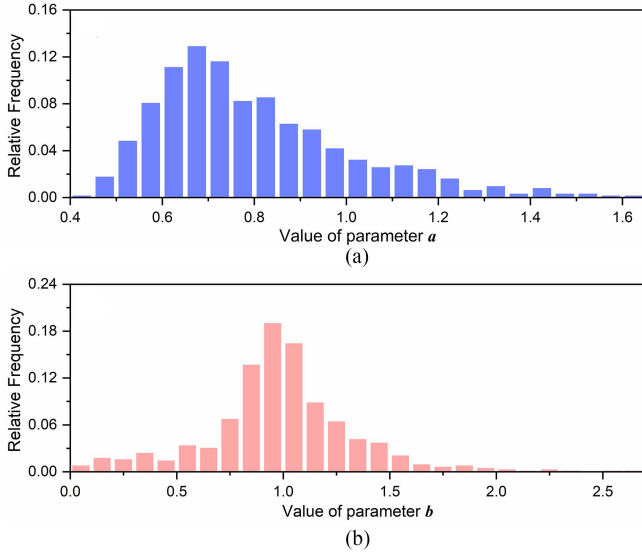
Fig. 10. Normalized histogram of (a) parameter a values, and (b) parameter b values.

TABLE II
STATISTICAL ANALYSIS OF PARAMETERS A AND B FOR TC CASES WITH
DIFFERENT INTENSITIES COLLECTED FROM NOAA FLIGHT MISSIONS

Statistics	Category	Number	Mean	Std	Range
	Small	301	0.90	0.21	0.53–1.66
a	Moderate	206	0.76	0.18	0.48–1.45
	Major	113	0.61	0.09	0.45–0.94
	Small	301	0.99	0.43	0.03–2.63
b	Moderate	206	1.01	0.32	0.10–2.34
	Major	113	0.93	0.13	0.32–1.66
	Small	301	67.75	39.17	2.5–149
R_{max} (km)	Moderate	206	56.92	34.28	14–149
	Major	113	30.06	16.14	11.15–123.5

Fig. 11 Scatter diagrams of (a) parameter a, (b) parameter b, and (c) R_{max} relative to the TC intensities (V_{max}), respectively. The colors indicate the categories of samples.

[0.65, 1.70]. Moreover, 78% of the cases are in the main range [0.50, 0.95]. In Fig. 10(b), parameter b's mean and Std values are 0.99 and 0.36, respectively. Similarly, its distribution range is [0, 2.6] with the maximum at the subinterval [0.9, 1.0], while 71% of the cases are in the main range [0.70, 1.30]. Finally, the SAR-calculated values of a and b in Table I are within the one-sigma range of the distributions in Fig 10, demonstrating that the parameters extracted from SAR images are reliable.

To explore the relationship between the model parameters (a, b, and R_{max}) and TC intensity (V_{max}), we divided the cases into three classes according to the hurricane categories defined by the Saffir–Simpson hurricane wind scale: the Small ($V_m < 33.1$ m/s) indicates the TC cases which are weaker than category 1, the moderate (33.1 m/s $\leq V_{max} < 49.2$ m/s) indicates those of categories 1 and 2, and the major ($V_{max} \geq 49.2$ m/s) represents those of categories 3 to 5. The distributions of parameters a, b, and R_{max} with TC intensity are shown in Fig. 11, and the corresponding statistical analysis results are given in Table II, including the mean, the Std, and the distribution range for
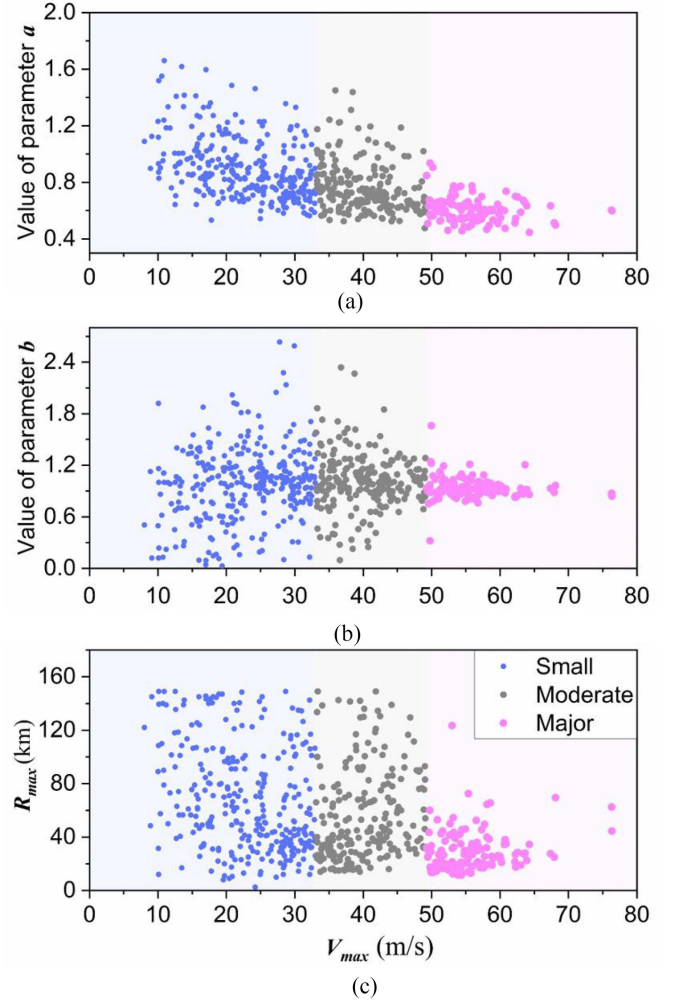
parameters. As seen from Fig. 11 and Table II, there is a decreasing trend for the value of parameter a with the TC intensity increasing from small to major. For parameters b and R_{max}, there is no such apparent dependence between their values and TC intensities. Moreover, for the small TCs, the value range of these three parameters is large and the corresponding distribution is discrete. For the Moderate TCs, the distribution of parameters a and b is significantly more compact, but that of R_{max} is almost unchanged. In contrast, these three parameters value of major TCs has a smaller fluctuation compared to the small and moderate ones, i.e., the parameter values of most cases are concentrated in a small range, especially for parameters a and b. The value of parameters determines the 2-D shape of TCs. In other words, if the parameter variation range is large, the shape difference of this kind of TCs will be large, otherwise, they have similar 2-D shapes. Therefore, according to the above statistical analysis results, the shape of Small TCs often varies greatly, which contains a lot of cases at the initial stage of formation or the end of extinction. However, the shape of major TCs is usually similar because the parameter changes of different

TCs are relatively small. This is reasonable because TCs with high intensity is usually the mature ones with relatively stable structures.

V. Conclusion

In this article, a novel tangential wind speed profile model, referred to as the TWP model, is proposed based on SAR observations, and the model functions are piecewise and nonlinear. Then, 11 SAR images covering 7 TCs are selected as the study cases, and the validation results indicate that the TWP model outperforms the commonly used SMRV model. Besides, the comparison against SFMR wind measurements also proves the suitability of the TWP model to reproduce the tangential wind behavior of TCs. Furthermore, a comprehensive characterization of the TWP-derived parameters a, b, and $R_{\max}$ shows a good correlation of the former with TC intensity, i.e., parameter a decrease with TC intensity or, in other words, steeper wind gradients inside the eyewall are found in stronger TCs, as expected. Interestingly, the Std values and distribution ranges of both a and b decrease with increasing TC intensity, leading to a similar (fixed) TWP shape for major TCs. The TWP model, therefore, proves to be a very effective tool for improved TC characterization and forecasting purposes.

In summary, the new model presents two main improvements with respect to the SMRV model: it effectively addresses the unsmooth transition of the tangential wind profile in the peak wind region; and it better fits the actual tangential wind speed profile as depicted by SAR and SFMR. These two advantages make it possible to estimate the TC tangential wind speed more accurately.

Similar to other existing tangential wind profile models, the TWP model assumes TC symmetry around its center, while TC tangential winds as well as the inflow/outflow winds are often asymmetric. In the future, we plan to combine the TWP model with an azimuth asymmetry model to describe the asymmetric TC winds.

Appendix

Reference [13] proposed the SMRV model with a decay exponent a, the model function is

$$\bar{V} = \begin{cases} \bar{V}_{\max} \left(\dfrac{r}{R_{\max}} \right) & r \le R_{\max} \\ \bar{V}_{\max} \left(\dfrac{R_{\max}}{r} \right)^{\alpha} & r \ge R_{\max} \end{cases}$$

where the $\bar{V}$, r, $\bar{V}_{\max}$, and $R_{\max}$ are the tangential wind speed, radius, maximum azimuthal-mean tangential wind speed, and the radius of maximum azimuthal-mean tangential wind, respectively. Specifically, α is the decay exponent, which represents the downward rate of tangential wind in the external wind field.

The model function of the revised SMRV model is

$$\bar{V} = \begin{cases} \left(\bar{V}_{\max} - V_{\text{center}} \right) \left(\dfrac{r}{R_{\max}} \right) + V_{\text{center}} & r \le R_{\max} \\ \bar{V}_{\max} \left(\dfrac{R_{\max}}{r} \right)^{\alpha} & r \ge R_{\max} \end{cases}$$

where the V_{center} is the wind speed at the center of the TC.

The Gauss vortex model has been used in [13], [41], and the model function is

$$\bar{V} = \bar{V}_{\max} \frac{1 + \sigma^{-2}}{r} \left[1 - \exp\left(-\frac{\sigma^2 r^2}{2} \right) \right]$$

where $\sigma \approx 1.58520$ satisfies the transcendental relation, $\exp(\frac{\sigma^2}{2}) - \sigma^2 - 1 = 0$.

References

[1] P. J. Vickery, F. J. Masters, M. D. Powell, and D. Wadhera, "Hurricane hazard modeling: The past, present, and future," *J. Wind Eng. Ind. Aerodyn.*, vol. 97, no. 7/8, pp. 392–405, Sep./Oct. 2009.

[2] G. J. Holland, "An analytic model of the wind and pressure profiles in hurricanes," *Monthly Weather Rev.*, vol. 108, no. 8, pp. 1212–1218, 1980.

[3] Y. Krien et al., "Can we improve parametric cyclonic wind fields using recent satellite remote sensing data?," *Remote Sens.*, vol. 10, no. 12, Dec. 2018, Art. no. 1963.

[4] M. C. Peng, L. Xie, and L. J. Pietrafesa, "Tropical cyclone induced asymmetry of sea level surge and fall and its presentation in a storm surge model with parametric wind fields," *Ocean Model.*, vol. 14, no. 1-2, pp. 81–101, 2006.

[5] N. Lin and D. Chavas, "On hurricane parametric wind and applications in storm surge modeling," *J. Geophys. Res.-Atmos.*, vol. 117, May 2012, Art. no. D09120.

[6] Y. Ding, T. D. Ding, A. Rusdin, Y. X. Zhang, and Y. F. Jia, "Simulation and prediction of storm surges and waves using a fully integrated process model and a parametric cyclonic wind model," *J. Geophys. Res.-Oceans*, vol. 125, no. 7, Jul. 2020, Art. no. e2019JC015793.

[7] Y. J. Kim, T. W. Kim, and J. S. Yoon, "Study on storm surge using parametric model with geographical characteristics," *Water*, vol. 12, no. 8, Aug. 2020, Art. no. 2251.

[8] L. Vijayan, W. R. Huang, K. Yin, E. Ozguven, S. Burns, and M. Ghorbanzadeh, "Evaluation of parametric wind models for more accurate modeling of storm surge: A case study of hurricane michael," *Natural Hazards*, vol. 106, no. 3, pp. 2003–2024, Apr. 2021.

[9] L. Xie, H. Q. Liu, B. Liu, and S. W. Bao, "A numerical study of the effect of hurricane wind asymmetry on storm surge and inundation," *Ocean Model.*, vol. 36, no. 1-2, pp. 71–79, 2011.

[10] L. Xie, S. W. Bao, L. J. Pietrafesa, K. Foley, and M. Fuentes, "A real-time hurricane surface wind forecasting model: Formulation and verification," *Monthly Weather Rev.*, vol. 134, no. 5, pp. 1355–1370, May 2006.

[11] P. Ruiz-Salcines, P. Salles, L. Robles-Diaz, G. Diaz-Hernandez, A. Torres-Freyermuth, and C. M. Appendini, "On the use of parametric wind models for wind wave modeling under tropical cyclones," *Water*, vol. 11, no. 10, Oct. 2019, Art. no. 2044.

[12] S. Wang et al., "An improved asymmetric hurricane parametric model based on cross-polarization SAR observations," *IEEE J. Sel. Topics Appl. Earth Observ. Remote Sens.*, vol. 14, pp. 1411–1422, Jan. 2021.

[13] K. J. Mallen, M. T. Montgomery, and B. Wang, "Reexamining the Near-core radial structure of the tropical cyclone primary circulation: Implications for vortex resiliency," *J. Atmos. Sci.*, vol. 62, no. 2, pp. 408–425, Feb. 2005.

[14] M. Sitkowski, J. P. Kossin, and C. M. Rozoff, "Intensity and structure changes during hurricane eyewall replacement cycles," *Monthly Weather Rev.*, vol. 139, no. 12, pp. 3829–3847, Dec. 2011.

[15] X. F. Yang, G. H. Liu, Z. W. Li, and Y. Yu, "Preliminary validation of ocean surface vector winds estimated from China's HY-2A scatterometer," *Int. J. Remote Sens.*, vol. 35, no. 11-12, pp. 4532–4543, 2014.

[16] K. S. Xiang, X. F. Yang, M. Zhang, Z. W. Li, and F. P. Kong, "Objective estimation of tropical cyclone intensity from active and passive microwave remote sensing observations in the northwestern pacific ocean," *Remote Sens.*, vol. 11, no. 6, Mar. 2019, Art. no. 627.

[17] G. S. Zhang, X. F. Li, W. Perrie, P. A. Hwang, B. Zhang, and X. F. Yang, "A hurricane wind speed retrieval model for C-Band RADARSAT-2 cross-polarization ScanSAR images," *IEEE Trans. Geosci. Remote Sens.*, vol. 55, no. 8, pp. 4766–4774, Aug. 2017.

[18] G. S. Zhang, W. Perrie, B. Zhang, J. S. Yang, and Y. J. He, "Monitoring of tropical cyclone structures in ten years of RADARSAT-2 SAR images," *Remote Sens. Environ.*, vol. 236, Jan. 2020, Art. no. 111449.

[19] S. H. Jin, X. F. Li, X. F. Yang, J. A. Zhang, and D. L. Shen, "Identification of tropical cyclone centers in SAR imagery based on template matching and particle swarm optimization algorithms," *IEEE Trans. Geosci. Remote Sens.*, vol. 57, no. 1, pp. 598–608, Jan. 2019.

[20] B. Zhang and W. Perrie, "Cross-Polarized synthetic aperture radar: A new potential measurement technique for hurricanes," *Bull. Amer. Meteorol. Soc.*, vol. 93, no. 4, pp. 531–541, Apr. 2012.

[21] H. Shen, W. Perrie, Y. J. He, and G. Q. Liu, "Wind speed retrieval from VH dual-polarization RADARSAT-2 SAR images," *IEEE Trans. Geosci. Remote Sens.*, vol. 52, no. 9, pp. 5820–5826, Sep. 2014.

[22] G. J. van Zadelhoff, A. Stoffelen, P. W. Vachon, J. Wolfe, J. Horstmann, and M. B. Rivas, "Retrieving hurricane wind speeds using cross-polarization C-band measurements," *Atmos. Meas. Techn.*, vol. 7, no. 2, pp. 437–449, 2014.

[23] J. Horstmann, S. Falchetti, C. Wackerman, S. Maresca, M. J. Caruso, and H. C. Graber, "Tropical cyclone winds retrieved from C-Band cross-polarized synthetic aperture radar," *IEEE Trans. Geosci. Remote Sens.*, vol. 53, no. 5, pp. 2887–2898, May 2015.

[24] P. A. Hwang et al., "Cross-polarization geophysical model function for C-band radar backscattering from the ocean surface and wind speed retrieval," *J. Geophys. Res.-Oceans*, vol. 120, no. 2, pp. 893–909, Feb. 2015.

[25] H. Shen, W. Perrie, and Y. J. He, "Evaluation of hurricane wind speed retrieval from cross-dual-pol SAR," *Int. J. Remote Sens.*, vol. 37, no. 3, pp. 599–614, Feb. 2016.

[26] A. A. Mouche, B. Chapron, B. Zhang, and R. Husson, "Combined co- and cross-polarized SAR measurements under extreme wind conditions," *IEEE Trans. Geosci. Remote Sens.*, vol. 55, no. 12, pp. 6746–6755, Dec. 2017.

[27] A. Mouche, B. Chapron, J. Knaff, Y. L. Zhao, B. Zhang, and C. Combot, "Copolarized and cross-polarized SAR measurements for high-resolution description of major hurricane wind structures: Application to irma category5 hurricane," *J. Geophys. Res.-Oceans*, vol. 124, no. 6, pp. 3905–3922, Jun. 2019.

[28] S. Wang, K.-V. Yuen, X. Yang, and B. Zhang, "A nonparametric tropical cyclone wind speed estimation model based on dual-polarization SAR observations," *IEEE Trans. Geosci. Remote Sens.*, vol. 60, 2022, Art. no. 4208213.

[29] V. T. Wood and L. W. White, "A new parametric model of vortex tangential-wind profiles: Development, testing, and verification," *J. Atmos. Sci.*, vol. 68, no. 5, pp. 990–1006, 2011.

[30] H. E. Willoughby, R. W. R. Darling, and M. E. Rahn, "Parametric representation of the primary hurricane vortex. Part II: A new family of sectionally continuous profiles," *Monthly Weather Rev.*, vol. 134, no. 4, pp. 1102–1120, Apr. 2006.

[31] G. S. Zhang, B. Zhang, W. Perrie, Q. Xu, and Y. J. He, "A hurricane tangential wind profile estimation method for C-band cross-polarization SAR," *IEEE Trans. Geosci. Remote Sens.*, vol. 52, no. 11, pp. 7186–7194, Nov. 2014.

[32] P. L. N. Murty, P. K. Bhaskaran, R. Gayathri, B. Sahoo, T. S. Kumar, and B. SubbaReddy, "Numerical study of coastal hydrodynamics using a coupled model for Hudhud cyclone in the bay of bengal," *Estuarine Coastal Shelf Sci.*, vol. 183, pp. 13–27, Dec. 2016.

[33] G. J. Holland, J. I. Belanger, and A. Fritz, "A revised model for radial profiles of hurricane winds," *Monthly Weather Rev.*, vol. 138, no. 12, pp. 4393–4401, Dec. 2010.

[34] T. Loridan, S. Khare, E. Scherer, M. Dixon, and E. Bellone, "Parametric modeling of transitioning cyclone wind fields for risk assessment studies in the western north pacific," *J. Appl. Meteorol. Climatol.*, vol. 54, no. 3, pp. 624–642, Mar. 2015.

[35] J. D. McCalpin, "On the adjustment of azimuthally perturbed vortices," *J. Geophysical Res.*, vol. 92, no. C8, pp. 8213–8225, 1987.

[36] J. W. Park, A. A. Korosov, M. Babiker, S. Sandven, and J. S. Won, "Efficient thermal noise removal for sentinel-1 TOPSAR Cross- Polarization Channel," *IEEE Trans. Geosci. Remote Sens.*, vol. 56, no. 3, pp. 1555–1565, Mar. 2018.

[37] R. Piantanida, N. Miranda, and N. Franceschi, *Thermal Denoising of Products Generated By the S-1 IPF*, 2017. [Online]. Available: https://sentinel.esa.int/documents/247904/2142675/

[38] E. W. Uhlhorn, P. G. Black, J. L. Franklin, M. Goodberlet, J. Carswell, and A. S. Goldstein, "Hurricane surface wind measurements from an operational stepped frequency microwave radiometer," *Monthly Weather Rev.*, vol. 135, no. 9, pp. 3070–3085, Sep. 2007.

[39] G. S. Zhang, C. Xu, X. F. Li, Z. Q. Zhu, and W. Perrie, "Tropical cyclone center and symmetric structure estimating from SMAP data," *IEEE Trans. Geosci. Remote Sens.*, vol. 60, 2022, Art. no. 4205311.

[40] G. S. Zhang, X. F. Li, W. Perrie, and J. A. Zhang, "Tropical cyclone winds and inflow angle asymmetry from SAR imagery," *Geophys. Res. Lett.*, vol. 48, no. 20, Oct. 2021, Art. no. e2021GL095699.

[41] R. W. Jones, H. E. Willoughby, and M. T. Montgomery, "Alignment of hurricane-like vortices on f and β planes," *J. Atmos. Sci.*, vol. 66, no. 6, pp. 1779–1792, Jun. 2009.

Sheng Wang received the B.S. degree in remote sensing science and technology from Wuhan University, Wuhan, China, in 2017, and the M.S. degree in electronic and communication engineering from Aerospace Information Research Institute, Chinese Academy of Sciences, Beijing, China, in 2020. He is currently working toward the Ph.D. degree in civil engineering with the University of Macau, Macau, China.

His current research interests include the machine learning in the application of ocean remote sensing.

Xiaofeng Yang (Senior Member, IEEE) received the B.S. degree in environmental science from Sichuan University, Chengdu, China, in 2005, and the Ph.D. degree in cartography and geographic information systems from the Institute of Remote Sensing Applications (IRSA), Chinese Academy of Sciences (CAS), Beijing, China, in 2010.

From 2009 to 2010, he was a Visiting Research Scientist with the Department of Atmospheric and Oceanic Science, University of Maryland, College Park, MD, USA. In 2010, he joined IRSA, CAS, where he became an Associate Professor in 2013 and a Full Professor in 2016. His research interests include satellite oceanography, synthetic aperture radar image processing, and marine atmospheric boundary layer process studies.

Dr. Yang is an Associate Editor for *Remote Sensing* and an Editorial Board Member for IEEE TRANSACTIONS ON GEOSCIENCE AND REMOTE SENSING. He is the Secretary General of the Technical Committee on Earth Science from Space, Chinese Society of Space Research.

Marcos Portabella was born in Barcelona, Spain, in 1970. He received the B.Sc. degree in physics from the University of Barcelona, Barcelona, Spain, in 1994, the M.Sc. degree in remote sensing from the Institute of Space Studies of Catalonia, Barcelona, Spain, in 1995, and the Ph.D. degree in physics from the University of Barcelona, Barcelona, Spain in 2002.

He is currently with the Institut de Ciències del Mar, Barcelona, Spain, where he is involved in satellite remote sensing, and particularly scatterometry and L-band radiometry.

Ka-Veng Yuen received the Ph.D. degree in civil engineering from the California Institute of Technology, Pasadena, CA, USA, in 2002.

He is a Distinguished Professor of Civil and Environmental Engineering, University of Macau, Macau, China. According to the citation ranking published in PLOS Biology in October 2019 by Prof. John P.A. Ioannidis of Stanford University, Prof. Yuen is among the top 125 Civil Engineering scholars worldwide. His research expertise includes Bayesian inference, uncertainty quantification, system identification, structural health monitoring, reliability analysis, and analysis of dynamical systems.

Yanlei Du received the B.S. degree in remote sensing science and technology from Chang'an University, Xi'an, China, in 2014, and the Ph.D. degree in cartography and geographic information systems from the Institute of Remote Sensing and Digital Earth, Chinese Academy of Sciences, Beijing, China, in 2019.

During his Ph.D. program (2017–2019), he was a Visiting Scholar with the Department of Electrical Engineering and Computer Science, University of Michigan, Ann Arbor, MI, USA. From 2019 to 2021, he was a Postdoctoral Research Fellow with the Department of Electronic Engineering, Tsinghua University, Beijing, China. He is currently an Assistant Professor with the State Key Laboratory of Remote Sensing Science, Aerospace Information Research Institute, CAS. His research interests include computational electromagnetics in applications of ocean remote sensing, radar polarimetry and satellite oceanography.

Miao Zhang received the B.S. degree in atmospheric science from Lanzhou University, Lanzhou, China, in 2009, and the Master's degree in atmospheric science from the Chinese Academy of Meteorological Sciences, Beijing, China, in 2012.

In 2012, she was with the National Satellite Meteorological Center, where she was an Assistant Researcher in 2015 and an Associate Researcher in 2020. Her research interests include satellite oceanography, retrieval of sea surface temperature and cloud top height from Fengyun satellite remote Sensing.